On AgRhO$_2$, and the new quaternary delafossites AgLi$_{1/3}$M$_{2/3}$O$_2$, syntheses and analyses of real structures

V. Todorova [a], A. Leineweber [b], L. Kienle [c], V. Duppel [a], M. Jansen [a,*]

[a] Max Planck Institute for Solid State Research, Heisenbergstr. 1, D-70569 Stuttgart, Germany
[b] Max-Planck-Institute for Metals Research, Heisenbergstr. 3, D-70569 Stuttgart, Germany
[c] Institute of Materials Research, Kaiserstr. 2, D-24143 Kiel, Germany

ABSTRACT

Two new quaternary delafossite type oxides with the general formula Ag(Li$_{1/3}$M$_{2/3}$)O$_2$, M=Rh, Ir, have been synthesized, and their structures characterized. Based on X-ray and electron diffraction analyses the structural similarity with AgRhO$_2$ delafossite, has been evidenced. The real structures of the quaternary delafossites have been revealed, which has allowed to fully explain the diffuse scattering as observed in X-ray powder diffraction. AgRhO$_2$ is thermally stable up to 1173 K, the behavior of the two quaternary compounds AgLi$_{1/3}$Rh$_{2/3}$O$_2$ and AgLi$_{1/3}$Ir$_{2/3}$O$_2$ is comparable, and they decompose above 950 and 800 K, respectively. AgRhO$_2$ shows temperature independent paramagnetism, while for the other two an effective magnetic moment of 1.77μ_B for Ir, and 1.70μ_B for Rh were determined, applying the Curie–Weiss law. All compounds are semiconducting with activation energies of 4.97 kJ mol^{-1} (AgLi$_{1/3}$Rh$_{2/3}$O$_2$), 11.42 kJ mol^{-1} (AgLi$_{1/3}$Ir$_{2/3}$O$_2$) and 17.58 kJ mol^{-1} (AgRhO$_2$).

© 2011 Elsevier Inc. All rights reserved.

1. Introduction

Delafossites [1], CuMO$_2$ and AgMO$_2$ [2,3] (see Fig. 1a), represent an extensive family of ternary oxides that provides appealing examples of charge [4], spin [5], and orbital ordering on trigonal lattices [6] and has recently attracted significant interest in the context of search for superior thermoelectric or (photo)catalytic [7] materials. In principle, any trivalent cation capable of adopting an octahedral coordination by oxygen may serve as the cationic component M in an "usual" ternary delafossite [3]. Surprisingly iridium, for which the oxidation state of 3+ is known to be one of its most favored, has not yet been successfully included in a delafossite arrangement. In addition to reasons of completing chemical systematics, a compound like AgIrO$_2$ should offer promising potential for catalytic processes involving oxygen. Our first attempts to directly synthesize AgIrO$_2$ in an all-solid-state reaction applying high oxygen pressure have failed, because of the intricate control of the oxygen pressure required: at a too low oxygen pressure silver oxide gets reduced to elemental silver, while at higher pressure phases containing Ir^{4+} result. Ion exchange of alkali oxometalates in molten silver nitrate/potassium nitrate has proven a versatile alternative to access ternary silver(I) oxides at thermally milder conditions. At treating Li$_2$IrO$_3$ with molten AgNO$_3$/KNO$_3$, a respective exchange of the

monovalent cations was indeed effected. However, only 3/4 of silver was substituted for lithium and iridium stayed in the Ir^{4+} state. The final product of composition AgLi$_{1/3}$Ir$_{2/3}$O$_2$, and the rhodium analog prepared along a similar procedure, represent quaternary variants of the delafossite structure type.

Analogous stannates [8] and titanates [8,9] were reported and qualitatively assigned to the delafossite structure family, previously. Significant features in X-ray powder diffraction (XRPD) patterns have remained unexplored. Here we report on the synthesis of AgRhO$_2$, and of two new representatives AgLi$_{1/3}$Ir$_{2/3}$O$_2$ and AgLi$_{1/3}$Rh$_{2/3}$O$_2$ of the quaternary 3R-delafossites. The average and defect structures of the latter have been analyzed, based on XRPD, considering diffuse scattering, and HRTEM.

2. Experimental part

2.1. Synthesis

For the synthesis of AgLi$_{1/3}$Ir$_{2/3}$O$_2$ and AgLi$_{1/3}$Rh$_{2/3}$O$_2$, Li$_2$RhO$_3$ and Li$_2$IrO$_3$ were treated with an excess of a molten mixture of AgNO$_3$ (Roth, 99%) and KNO$_3$ (Merk 99.9%) in a ratio of 2:1. That reaction was performed in a sealed glass tube under Ar at 623 K for 350 h. Li$_2$RhO$_3$ was prepared by reacting stoichiometric mixtures of RhO$_2$ and LiOH (Alfa Aesar, anhydrous, 99.9%). The mixture was carefully ground and heated in a corundum crucible at 1123 K in an oxygen flow, for 48 h. RhO$_2$ was synthesized using high pressure oxygen autoclaves, starting from Rh(NO$_3$)$_3 \cdot x$H$_2$O
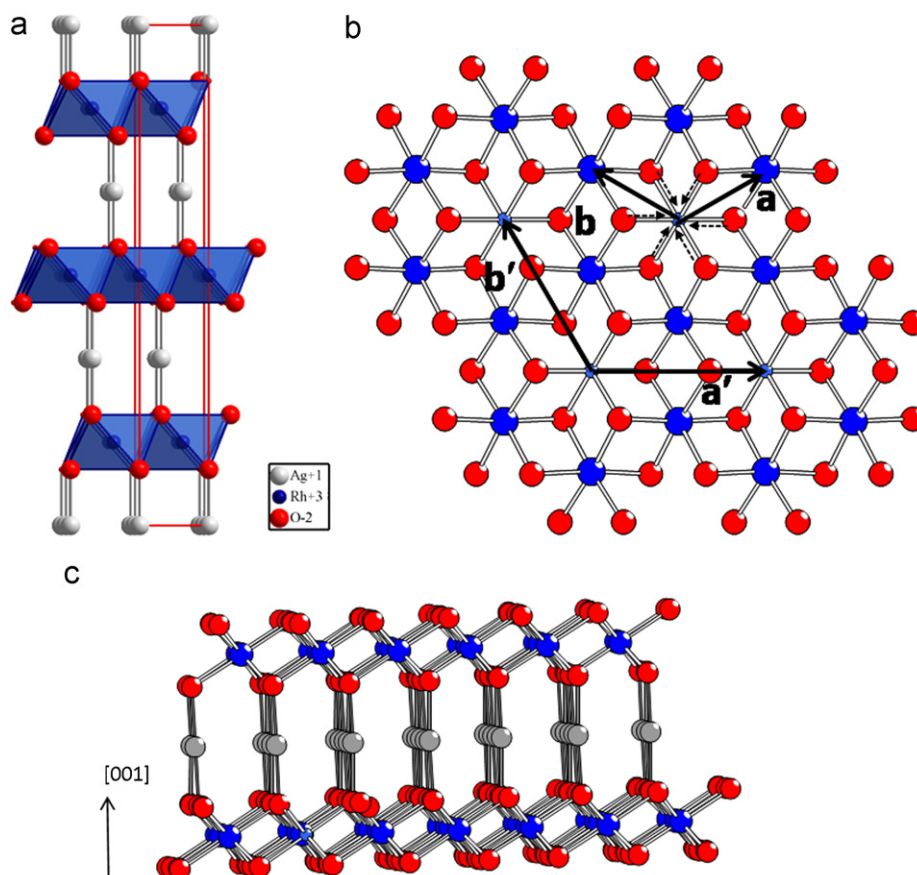
Fig. 1. (a) Delafossite structure $3R$ ($R\bar{3}m$), with $M=$Rh showing the RhO_6 octahedra, view along [010] direction; (b) one honeycomb-like ordered $[M_2LiO_6]^{3-}$ layer ($M=$Rh, Ir) together with the lattice basis vectors **a**, **b**, **a**′ and **b**′ (see text) as well as distortion in the oxygen partial structure indicated by dashed arrows as occurring around one Li atom (c) stacking of two layers with Ag in between.

(ChemPur, 36% Rh), which was decomposed in air at 473 K. The obtained amorphous residue was treated at 50–70 MPa oxygen pressure and at a temperature of 723 K, for 60 h. Li_2IrO_3 was synthesized along a similar procedure from LiOH (Alfa Aesar, anhydrous 99.9%) and IrO_2 (Alfa Aesar, 99.9%). $AgRhO_2$ was synthesized from $LiRhO_2$ by ion exchange at the same conditions as applied to the quaternary compounds. For the synthesis of $LiRhO_2$, stoichiometric amounts of Rh_2O_3 (Alfa Aesar, 99.9%) and LiOH (Alfa Aesar, anhydrous 99.9%) were mixed and heated in oxygen flow at 1123 K for 48 h.

2.2. Powder X-ray diffraction

XRPD investigations on $AgRhO_2$, $AgLi_{1/3}Ir_{2/3}O_2$ and $AgLi_{1/3}Rh_{2/3}O_2$ powders were performed using a D8-Advance from Bruker AXS, equipped with a Ge (111)—Johansson monochromator, Cu$K\alpha_1$ ($\lambda=1.540598$ Å). The powders were finely ground and filled in capillaries of 0.1 mm diameter. The data were collected in the 2θ range from 10° to 100°, with a step width of 0.01°. The average structures were refined using the software package TOPAS [10,11], while the patterns taking into account the defect structure were simulated using the DIFFAX software [12].

2.3. Transmission electron microscopy

For transmission electron microscopy, bulk samples of $AgRhO_2$, $AgLi_{1/3}Rh_{2/3}O_2$ and $AgLi_{1/3}Ir_{2/3}O_2$ were ground and dispersed in n-butanol. One drop of the suspension was placed on holy-carbon copper grids which serve as supports. TEM was performed with a Philips CM30ST microscope (300 kV, LaB$_6$

cathode, $C_S=1.15$ mm) which was equipped with a Spinning Star device [13] for applying precession electron diffraction (PED [14], maximum precession angle: 3°) and a Si/Li detector (Noran, Vantage System) for EDX analysis. HRTEM micrographs (multi-slice formalism) and SAED patterns were simulated with the EMS program packages [15] (spread of defocus: 70 Å, illumination semiangle: 1.2 mrad) and Emap [16]. All images were evaluated (including Fourier filtering) with the program Digital Micrograph 3.6.1 (Gatan) or Crisp (Calidris).

2.4. Quantitative analysis

Quantification of Ag, Li, Rh and Ir was performed via ICP-OES (Vista-Pro, CCD detector with axial plasma, Varian). 5 mg of a respective sample was treated in 5 ml concentrated HNO_3 in order to extract lithium and silver. The solid residue was digested in $HClO_4$ for rhodium/iridium determination, using a Berghof-Pressure-System with PTFE coating.

The analysis of oxygen was performed using a TC-436 (Leco, St. Joseph, MI, USA) with a He-flushed electrode chamber and I.R. cell (for detection of CO_2), employing SiO_2 as a standard.

2.5. Thermal analysis

Thermal analyses were carried out using the DTA/TG device STA 409, Netzsch. The sample was placed in a corundum crucible and heated at a rate of 5 K/min from 298 to 1173 K, under dry argon atmosphere.

2.6. Electronic conductivity measurement

The specific resistivity was measured applying the four-point-probe method with a self-assembled device (Chemistry service group, MPI FKF Stuttgart). The sample was cooled with a cryostat (Kryovac, Fa. Keithley). The current was measured by a digital multimeter (Fa. Keithley), and the voltage was monitored by a nano voltmeter (HP 4208, Fa. Hewlett Packard).

2.7. SQUID measurement

The magnetic response of $AgRhO_2$, $AgLi_{1/3}Rh_{2/3}O_2$ and $AgLi_{1/3}Ir_{2/3}O_2$ was studied on a SQUID-Magnetometer (SQUID-Superconducting Quantum Interference Device, MPMS 5.5. Fa. Quantum Design). 85.9, 67.2, and 129.7 mg, respectively, were placed in a gelatin capsule and measured with different magnetic fields in the temperature range between 2 and 360 K.

3. Structure determination

The XRPD patterns of $AgLi_{1/3}Ir_{2/3}O_2$ and $AgLi_{1/3}Rh_{2/3}O_2$ as well as of $AgRhO_2$ (Fig. 2) are very similar, and can be interpreted in terms of a rhombohedral 3R-delafossite-type of structure. Rietveld refinements were performed with a corresponding structure model, allowing for a common isotropic atomic displacement parameter for all atoms. Moreover, in order to describe the large widths of reflections with simultaneously high squared components (h^2+k^2+hk) and l^2 ($hk0$ and $00l$ reflections are relatively narrow), anisotropic microstrain broadening was considered [17,18]. This was done by convoluting the isotropic line broadening contributions by an anisotropic Voigtian one. This has Gaussian and Lorentzian parts showing full-width at half-maximum (FWHM) values of $B_{G,\Delta 2\theta_{hkl}} = 360°/\pi(1-\zeta)\tan\theta_{hkl}w_\varepsilon$ and $B_{L,\Delta 2\theta_{hkl}} = 360°/\pi\zeta\tan\theta_{hkl}w_\varepsilon$, where $0 \leq \zeta \leq 1$ is a fitting parameter determining the shape of the microstrain broadening, and where w_ε is some hkl-dependent width parameter of the microstrain distribution along the diffraction vector, which is identical to the FWHM in case of $\zeta = 0$ and 1. The width parameter is calculated according to

$$w_\varepsilon = \left(Z_{1111}\left(1-x_3^2\right)^2 + 6Z_{1133}\left(1-x_3^2\right)x_3^2 + Z_{3333}x_3^4\right)^{1/2}$$

with in principle refinable Z_{1111}, Z_{1133} and Z_{3333}, and where x_3 is the component parallel to c-axis of a unit vector parallel to the diffraction vector in the crystal frame of reference. In order to avoid strong correlations between the parameters describing the isotropic, largely instrumental line broadening contribution (not independently assessed) and the Z_{iijp} parameters, the parameter Z_{3333}, representing the – in all present cases smallest – microstrain broadening for $[00l]$ reflections, was in all cases held at $Z_{3333} = 0$. Since thus some part of the microstrain broadening may be incorporated into the description for isotropic line broadening, the refined Z_{1111} and Z_{1133} may be somewhat too small.
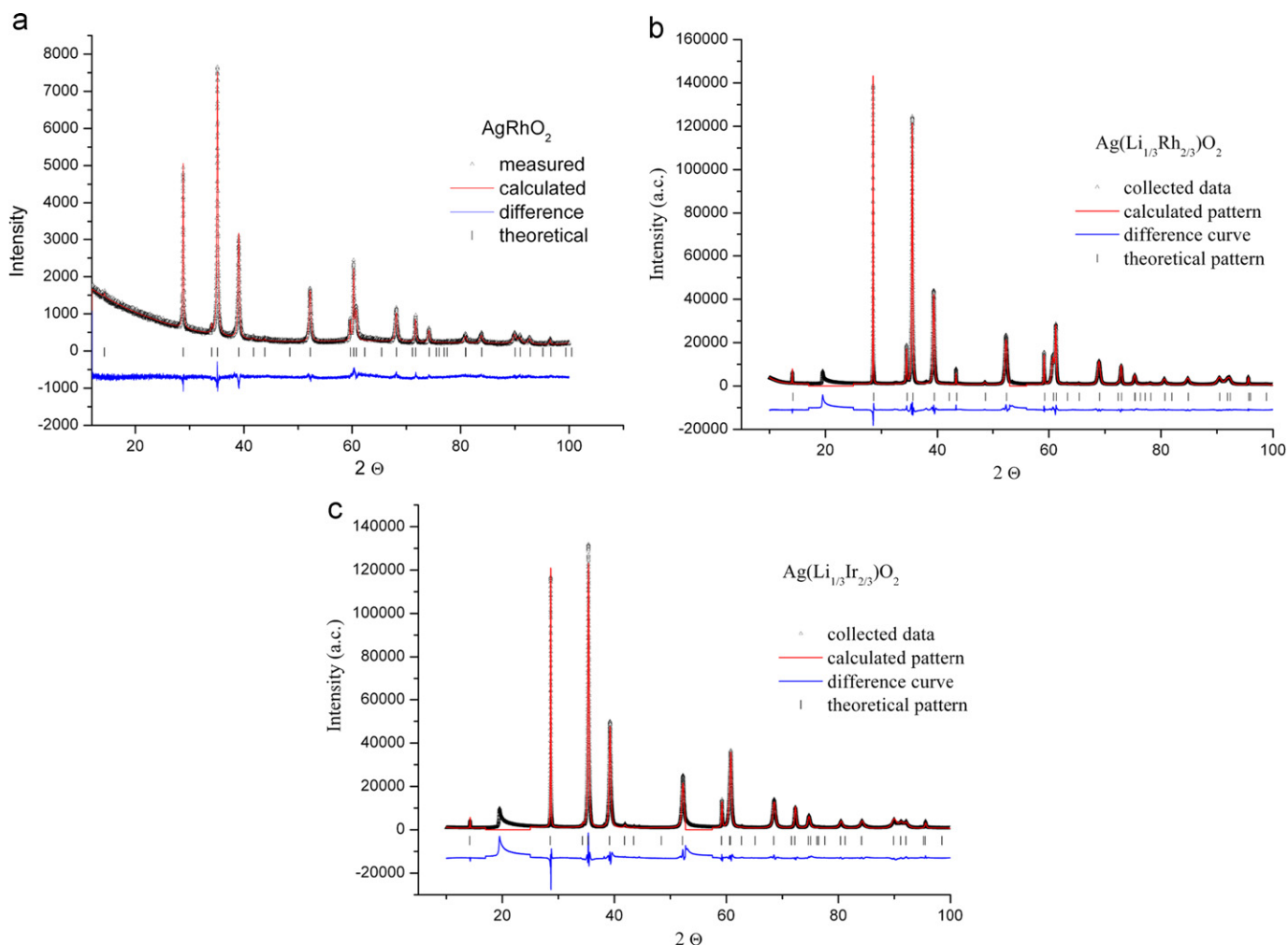

Fig. 2. Rietveld refinement of (a) $AgRhO_2$, (b) $Ag(Li_{1/3}Rh_{2/3})O_2$ and (c) $Ag(Li_{1/3}Ir_{2/3})O_2$.

For $AgLi_{1/3}Ir_{2/3}O_2$ and $AgLi_{1/3}Rh_{2/3}O_2$ a mixed occupation of the octahedral M metal sites by Rh and Li was additionally considered by refining the corresponding occupancies, keeping the sum of occupancies of both species to one. The details of the measurements and the refinements are listed in Table 1, and the refined fractional coordinates, occupancies, atomic displacement parameters are listed in Table 2. Some characteristic interatomic distances are listed in Table 3.

In spite of the above-mentioned similarity of all diffraction patterns, those of the quaternary delafossites $AgLi_{1/3}Ir_{2/3}O_2$ and $AgLi_{1/3}Rh_{2/3}O_2$ show with respect to $AgRhO_2$ some additional reflection-like features, in particular one at a diffraction angle of about $2\theta = 19.5°$. This feature cannot be explained by the applied $3R$-delafossite structure models with lattice parameters a and c. Strikingly, two of such features can be indexed with the non-integer indices $1/3\ 1/3\ 0\ (19.5°)$ and $4/3\ 1/3\ 0\ (53.5°)$ (all indexing is with respect to the unit cell of $AgRhO_2$), which would suggest a hexagonal/trigonal superstructure with $a' = b' = 3^{1/2}a$. However, the shape of these reflections (well visible for the $2\theta = 19.5°$ feature) with a steep drop of the intensity at the low-angle side (see Fig. 2) is typical for what is occasionally called *Warren peaks* [19], frequently observed for layered structures with irregular stacking sequences. These Warren peaks originate from rods of diffuse scattering occurring in reciprocal space perpendicular to the layer plane. If such a rod does not intersect the origin of the reciprocal space, the pertaining diffuse scattering will show a maximum in a powder-diffraction pattern at such a diffraction angle, which corresponds to a $1/d$ value representing the minimum distance of the rod to the origin of the reciprocal space. This

occurs even if the intensity on that rod in reciprocal space does not show a maximum at that minimum-distance point. Starting from high reflection angles the intensity will rise until a specific cut-off angle is approached, at which the intensity contribution pertaining to that rod will drop to zero. The above-mentioned indexing of the Warren peaks suggests that the rods of diffuse scattering occur at $h\ k\ l$ with $h = (3n \pm 1)/3$, $k = (3m \pm 1)/3$ (with integer n, m) and arbitrary l.

For the quaternary delafossites a real-structure model, which would explain occurrence of these Warren peaks, can be obtained assuming that the $2/3\ M^{4+}$ (M=Rh, Ir) and $1/3\ Li^+$ are occupying the octahedral sites. The most straightforward way to distribute these atoms within one layer $[M_2LiO_6]^{3-}$ is to follow a honey-comb-like ordering pattern, which leads to a two-dimensional $a' = b' = 3^{1/2}a$ superstructure for the M atoms (Fig. 1b). Since apparently no superstructure reflections can be discerned in the XRPD pattern, one may assume as a first approximation that these ordered $[M_2LiO_6]^{3-}$ layers are stacked within the framework of

Table 3
Bond length in $AgRhO_2$, $Ag(Li_{1/3}Rh_{2/3})O_2$ and $Ag(Li_{1/3}Ir_{2/3})O_2$.

Bond type	Bond length (Å)		
	$AgRhO_2$	$Ag(Li_{1/3}Rh_{2/3})O_2$	$Ag(Li_{1/3}Ir_{2/3})O_2$
Ag–O	2.0167(45)	2.0557(12)	1.9631(23)
Rh–O	2.0759(23)	2.04170(62)	
Ir–O			2.1071(12)
Li–O		2.04170(62)	

Table 1
Crystallographic and refinement details for $AgRhO_2$, $Ag(Li_{1/3}Rh_{2/3})O_2$ and $Ag(Li_{1/3}Ir_{2/3})O_2$ refined by the Rietveld method.

Molecular formula	$AgRhO_2$	$Ag(Li_{0.2803}Rh_{0.7197})O_2$	$Ag(Li_{0.3528}Ir_{0.6472})O_2$
Formula weight (in g/mol)	242.77	215.87	266.75
Space group	$R\bar{3}m$ (**166**)	$R\bar{3}m$ (**166**)	$R\bar{3}m$ (**166**)
a (Å)	3.06882(5)	3.02085(1)	3.04779(4)
c (Å)	18.59067 (4)	18.70306(0)	18.73348 (4)
V (Å^3)	151.624(6)	147.808(1)	150.702(4)
Z	3	3	3
Calc. density (g cm^{-3})	7.9763(3)	7.275(1)	8.817(4)
Temperature (K)	293	293	293
Wavelength (Å)	1.5406	1.5406	1.5406
R_{exp} (%)	4.35	2.00	1.87
R_p (%)	4.76	5.72	7.99
R_{wp} (%)	6.46	7.97	10.87
gof	1.48	3.97	5.80
$R(F^2)$ (%)	3.36	1.96	3.54
Starting angle (deg 2θ)	10	10	10
Final angle (deg 2θ)	100	100	100
Step width (deg 2θ)	0.01	0.01	0.01
Scan time (h)	40	40	40
Z_{1111} (10^{-6})	0.16(7)	9.6(1)	8.3(2)
Z_{1133} (10^{-6})	67(2)	158.9(6)	157(1)
ζ	0.57(1)	0.407(2)	0.520(4)
No. of variables	24	28	29

Table 2
Atom parameters for $AgRhO_2$, $Ag(Li_{1/3}Rh_{2/3})O_2$ and $Ag(Li_{1/3}Ir_{2/3})O_2$.

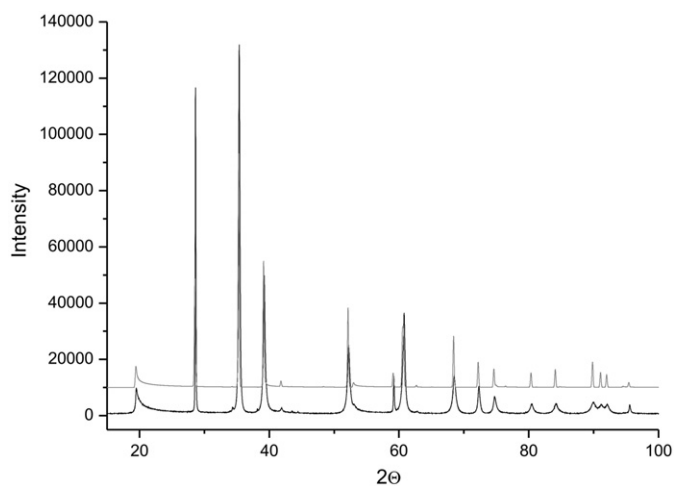| Atom	Wyckoff positions	x	y	$AgRhO_2$		$Ag(Li_{1/3}Rh_{2/3})O_2$		$Ag(Li_{1/3}Ir_{2/3})O_2$	
				z	Occ.	z	Occ.	z	Occ.
Ag	$3a$	0	0	0	1	0	1	0	
Li	$3b$	0	0			0.5	0.2803(6)	0.5	0.3528(8)
Rh	$3b$	0	0	0.5	1	0.5	0.7197(6)		
Ir	$3b$	0	0					0.5	0.6472(8)
O	$6c$	0	0	0.1084(2)	1	0.10991(7)	1	0.1047(1)	

Fig. 3. Comparison of the measured XRPD pattern of $Ag(Li_{1/3}Ir_{2/3})O_2$ (black) with a pattern simulated using DIFFAX [12] (gray, shifted by +10,000) assuming a random stacking sequence of two-dimensional honeycomb-like ordered $[M_2LiO_6]^{3-}$ layers ($M=Rh$, Ir; see Fig. 1b).

the delafossite structure in a completely random fashion. This can be achieved by shifting the layer placed upon a given layer along the stacking direction [001] by any of the vectors $\mathbf{s}_1=(\mathbf{a}+\mathbf{b})/3$, $\mathbf{s}_2=-\mathbf{a}/3$ or $\mathbf{s}_3=-\mathbf{b}/3$ with equal probability (compare Fig. 1b). Note that if the O atom arrangements of all the $[M_2LiO_6]^{3-}$ layers are mirrored on a plane containing the M and Li atoms, the signs of these vectors have to be inverted; but see also discussion in Section 4. XRPD patterns corresponding to such random stacks were simulated using the DIFFAX software and show good agreement with the experimental patterns, in particular with respect to the Warren peaks [12] (Fig. 3).

An approximant structure model employing a periodic sequence of the mentioned shift vectors was set up to calculate SAED patterns as well as HRTEM images. Indeed, the TEM investigations on $AgRhO_2$, $AgLi_{1/3}Rh_{2/3}O_2$ and $AgLi_{1/3}Ir_{2/3}O_2$ confirm on single-crystal-type information the crystal structure models derived from XRPD. Nanoprobe EDX indicates the presence of Li atoms inside the $[M_2LiO_6]^{3-}$ octahedral layers. The ratio Ag:M was found significantly larger than 1 for the quaternary materials. In the case of $AgLi_{1/3}Rh_{2/3}O_2$ the average of five point analyses performed on distinct crystallites gives Ag:Rh=1.37(3), while for $AgRhO_2$ the ratio was determined to be 0.95(2) (three measurements). Both values are slightly smaller than the expected ones, 1.5 and 1.0, respectively, based on the nominal compositions.

The metrics of the single crystalline fragments of $AgRhO_2$ were examined for their consistence with calculated data via extended tilting series. The tilt angles between [211], [241], [541], [841], [8–21] were determined to be 24.9°, 24.6°, 17°, 33° in good agreement with the calculated values of 25.4°, 24.2°, 17.4° and 33°. Moreover, all d-values agree with the calculated ones within experimental errors. In the following, the metrics of $AgRhO_2$ are used for the indexing of the $AgLi_{1/3}Rh_{2/3}O_2$ diffraction pattern since these structures are highly related.

Fig. 4 displays a comparison of the PED patterns of $AgRhO_2$ (left column) and $AgLi_{1/3}Rh_{2/3}O_2$ (right column). The attached simulated patterns for $AgRhO_2$ based on its "normal" delafossite-type structure convincingly match the experimental data, thus confirming the trigonal structure model on single crystals. In the case of $AgLi_{1/3}Rh_{2/3}O_2$ the fundamental reflections remain unchanged; however, additional intensities occur in the PED patterns, cf. additional spots (zone axes: [42-3], [48-3], [45-3], Fig. 4c–e) and the diffuse streaks for the zone axis pattern along

[210] Fig. 4b.[1] Indeed these features are well predicted by the approximant superstructure model.

Note, that the assumed two-dimensional ordering of $AgLi_{1/3}Rh_{2/3}O_2$ is not seen in *all* structure projections, as exemplified by the diffraction pattern of $AgLi_{1/3}Rh_{2/3}O_2$, which resembles the pattern of pure $AgRhO_2$ along [100] (cf. Fig. 4a, right vs. left). This contrasts to all zone axes where the honeycomb ordering is clearly seen in the structure projection, and where additional spots are present in the diffraction patterns. According to the real structure model, these spots are intersections of diffuse rods and the Ewald sphere, and not superstructure reflections, e.g. [241], [841] and [541] (Fig. 4c–e). Consequently, the intersections exhibit significant extension in the reciprocal space above and below the zero order Laue zone (ZOLZ). To image these contributions, PED is the method of choice [20], as demonstrated by the comparison of SAED and PED patterns depicted in Fig. 5. The diffuse rods are in-plane for the zone axis [210], thus SAED and PED patterns both show extended diffuse streaks on the positions $\pm x$ ($-1/3$ $2/3$ l) with $x\neq 3n$ (with n being an integer; cf. Fig. 5a). When tilting the sample perpendicular to $\mathbf{c}^*$ by ca. 19° (zone axis [20101], Fig. 5b) the observable diffuse intensity is minimized and spots appear at the positions of intersections for SAED. In the PED patterns, the intersections appear elongated by the diffuse contributions above and below the ZOLZ, and the extension of the diffuse streaks scales with the precession angle. Thus PED enables to identify structural disordering even for the cases where disordering is not detected by techniques like SAED and HRTEM which are interrelated with the projection of the structure.

For the zone axis [210], HRTEM was applied to prove the real-space structure model based on two dimensional ordering (cf. Fig. 6). In the case of the ordered crystals of $AgRhO_2$, the HRTEM micrographs convincingly match simulated images based on the trigonal structure model (Fig. 6a). For $AgLi_{1/3}Rh_{2/3}O_2$ (and analogously for $AgLi_{1/3}Ir_{2/3}O_2$) the shifts of adjacent octahedral sheets are clearly visible, cf. horizontal lines with dark ($\Delta f=-25$ nm, Fig. 6b, top right) and white spots ($\Delta f=-90$ nm, Fig. 6b, bottom right). A comparison of simulated micrographs and the projected potential indicates that these spots correlate with the honeycomb ordering of Li and Rh atoms inside the octahedral sheets. For $\Delta f=-25$ nm, the imaging conditions of Scherzer focus are approximated, hence, the black spots correlate with the pairs of Rh atoms inside the ordered $[Rh_2LiO_6]^{3-}$ sheets. The distinct positions of the sheets are highlighted by the marks inside the projection of the approximant supercell structure (Fig. 6c) and the corresponding marks inside the simulated micrographs (Fig. 6b).

4. Results and discussion

The title compounds were synthesized via ion exchange from $LiRhO_2$, Li_2RhO_3 and Li_2IrO_3, respectively, with molten mixtures of $AgNO_3/KNO_3$ in sealed glass ampoules. The obtained powders are black, and stable towards air and water. The thermal stability of the three samples was studied by means of DTA-TG in an inert atmosphere. The decomposition is accompanied by loss of oxygen. $AgRhO_2$ is thermally stable up to 1173 K, the behavior of the two quaternary compounds $AgLi_{1/3}Rh_{2/3}O_2$ and $AgLi_{1/3}Ir_{2/3}O_2$ is comparable, and they decompose above 950 and 800 K, respectively (Figs. 1–3 from the SI).

The magnetic response was recorded in the temperature interval from 3 to 360 K. $AgLi_{1/3}Rh_{2/3}O_2$, $AgLi_{1/3}Ir_{2/3}O_2$ are paramagnetic obeying the Curie–Weiss law in the temperature range

---

[1] All these phenomena were also observed with the stationary electron beam of the SAED technique.
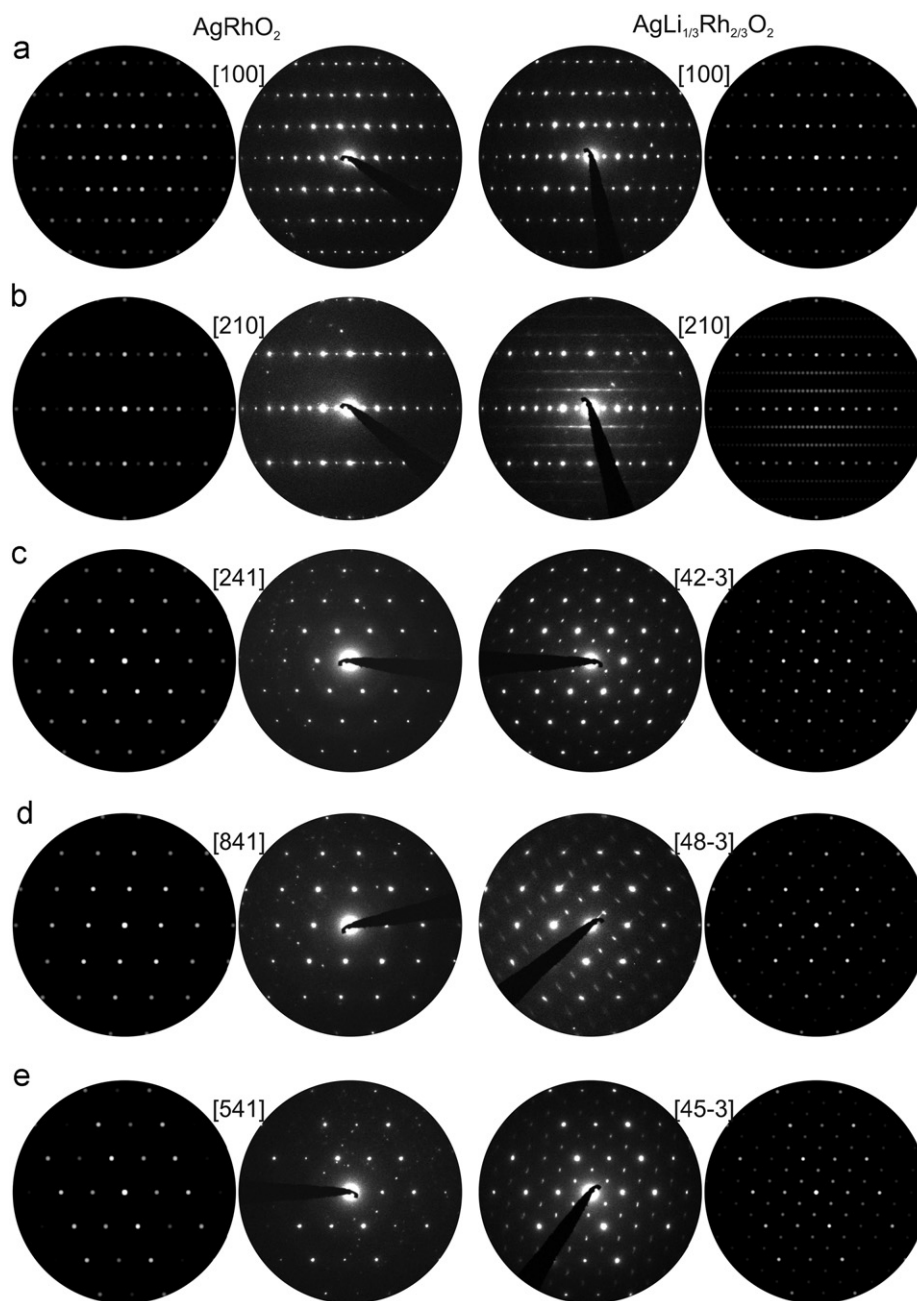
Fig. 4. PED patterns for AgRhO$_2$ (column b) and AgLi$_{1/3}$Rh$_{2/3}$O$_2$ (column c) with simulated PED patterns (columns a and d, respectively; zone axis specified in the figure) on the basis of the delafossite structure (AgRhO$_2$) and the approximant supercell structure (AgLi$_{1/3}$Rh$_{2/3}$O$_2$).

of 150–360 K. From a respective evaluation effective magnetic moments of 1.77 μ_B for Ir, and 1.70 μ_B for Rh were calculated (Fig. 7a and b). These numbers agree well with the spin-only value of 1.73 μ_B for the low-spin configurations of $4d^5$ and $5d^5$ ions. AgRhO$_2$ shows almost constant magnetic susceptibility in a quite wide temperature range (temperature independent paramagnetism (TIP)), with a slight Curie tailing, analogous to NaCoO$_2$ and AgCoO$_2$ [21]. The percentage of the Curie impurity as well the temperature-independent term, was calculated for the three fields of 1, 3 and 7 T. The TIP was found to be 3.91×10^{-5} cm^3 mol^{-1}, whereas the Curie impurities were estimated to 2%, of $S=1/2$, species.

The electronic conductivity of AgRhO$_2$ and Ag(Li$_{1/3}$M$_{2/3}$)O$_2$, $M=$Rh and Ir was measured in the temperature interval 2–300 K. All three compounds are semiconducting. The activation energies

derived are 4.97 kJ mol^{-1} (AgLi$_{1/3}$Rh$_{2/3}$O$_2$), 11.42 kJ mol^{-1} (AgLi$_{1/3}$Ir$_{2/3}$O$_2$) and 17.58 kJ mol^{-1} (AgRhO$_2$). In all cases resistivity drops at cooling by three to four orders of magnitude over the temperature range considered. The conductivities at 300 K are 9.0 S cm^{-1} (Ag(Li$_{1/3}$Rh$_{2/3}$)O$_2$), 1.7×10^{-2} S cm^{-1} (Ag(Li$_{1/3}$Ir$_{2/3}$)O$_2$) and 7.4×10^{-6} S cm^{-1} (AgRhO$_2$).

AgRhO$_2$ crystallizes in the 3R-delafossite type of structure with refined cell parameters of $a=3.06882(5)$ Å, $c=18.59067(4)$ Å, $Z=3$ and $V=151.624(6)$ Å. The Rh^{3+} cations are coordinated by six oxygen atoms (Rh–O distance equal to 2.076(2) Å), forming trigonally distorted edge-sharing octahedra, which build layers. The silver atoms are linearly coordinated by two oxygen atoms, parallel to the c-axes with bond lengths of 2.017(5) Å. All bond lengths and distances are as expected.

The new quaternary delafossites $Ag(Li_{1/3}Rh_{2/3})O_2$ and $Ag(Li_{1/3}Ir_{2/3})O_2$ display average structures, which are analogs to the $3R$ delafossite structure with disordered occupation of the above-mentioned O octahedral by Li and Rh/Ir. Analysis of the real structures, based on X-ray powder- and electron diffraction has revealed that within $[M_2LiO_6]^{3-}$ octahedral layers perpendicular to the c-axis of the delafossite structure a two-dimensional honeycomb ordering of Li vs. M occurs (see Section 3 and Fig. 1a). This ordering of Li vs. M will definitely lead to some displacements of the O atoms in order to optimize the Li–O and M–O distances, as e.g. indicated in Fig. 1b. Upon stacking the octahedral layer in a delafossite type fashion, these displacements will enforce some O–O connection lines between two adjacent layers not to be exactly parallel [001], although an O–Ag–O angle of 180° can still be achieved (see Fig. 1c). However, the Bragg
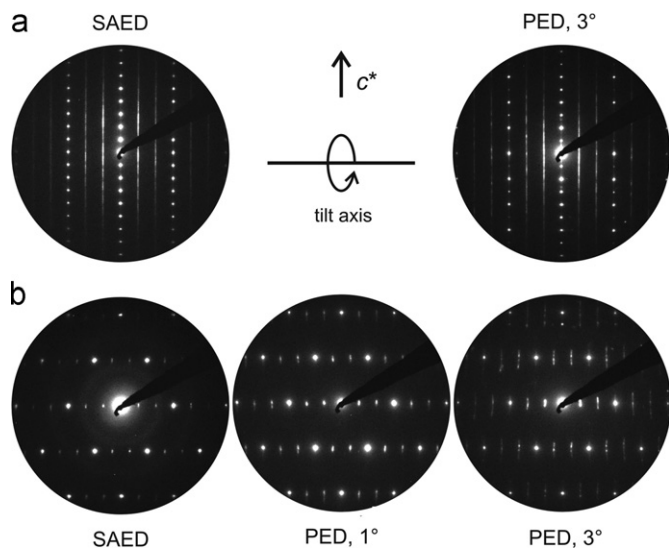

Fig. 5. (a) SAED (left) and PED pattern (precession angle 3°), zone axis [210]; (b) SAED (left) and PED patterns (center and right) after tilting the sample perpendicular to c^*. For the PED patterns, a precession angle of 1° (center) and 3° (right) was adjusted.
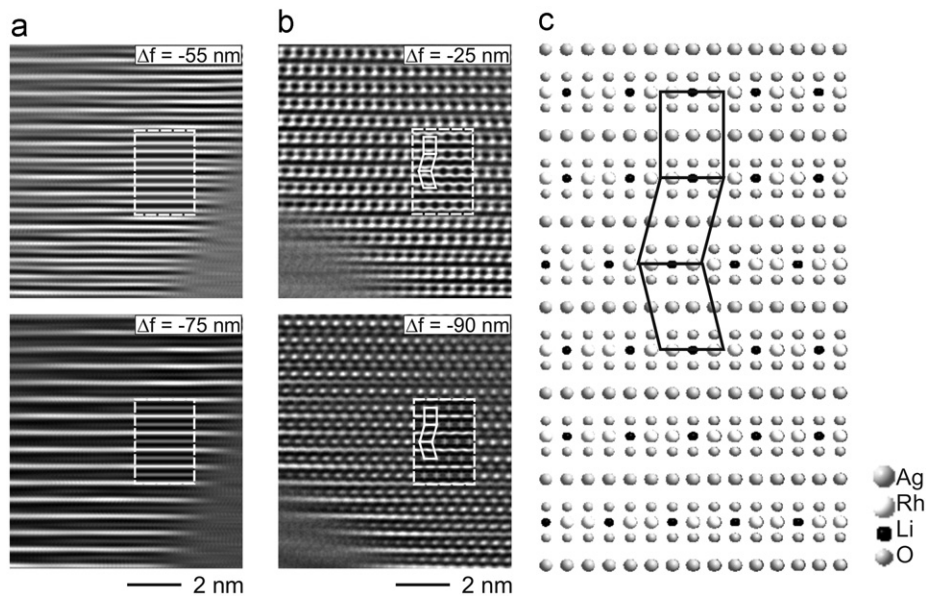

Fig. 7. Inverse molar susceptibilities of (a) $AgLi_{1/3}Rh_{2/3}O_2$ and (b) $AgLi_{1/3}Ir_{2/3}O_2$, as function of temperature.

Fig. 6. HRTEM micrographs recorded on (a) $AgRhO_2$, zone axis [210] with inserted simulation, assumed thickness: 2.7 nm and (b) $AgLi_{1/3}Rh_{2/3}O_2$, assumed thickness: 4.8 nm. (c) Projection of the supercell structure.

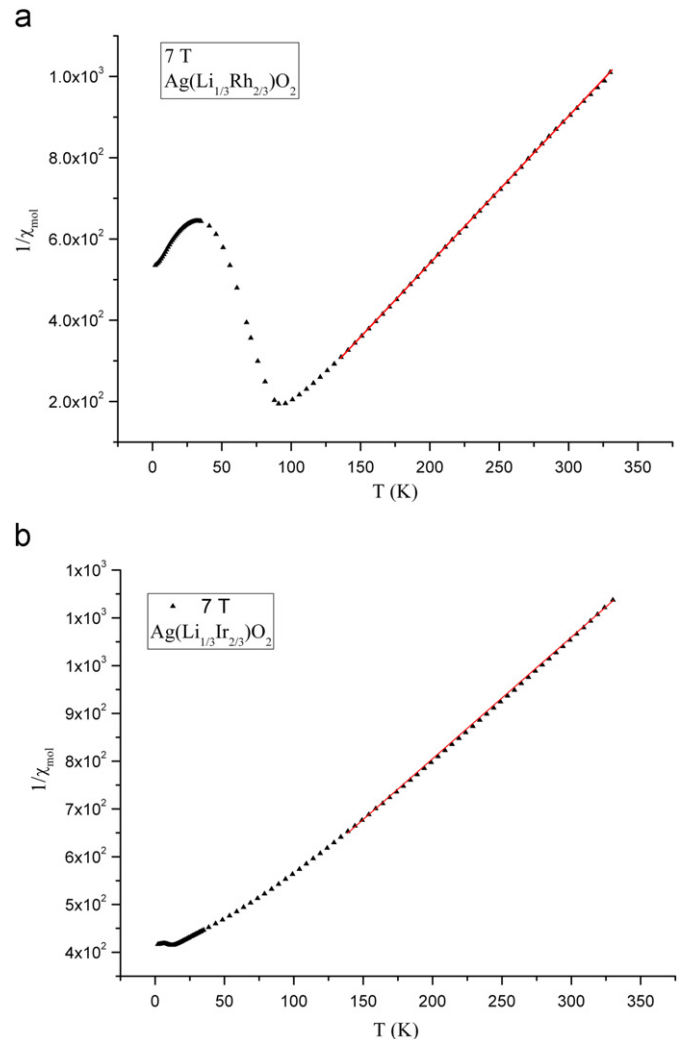reflections of the X-ray diffraction data do not provide sufficient information to determine independently the Li–O and M–O distances due to the disordered stacking of the octahedral layers leading to absence of superstructure/polytype reflections.

This disordered stacking occurs with the randomly occurring shift vectors $\mathbf{s}_i$ ($i=1, 2, 3$) ensuring a $3R$ delafossite type structure (see Section 3). With reference to the oxygen atoms this stacking can be described as ---AABBCCAA--- where the cyclic AB, BC and CA transitions occur between the O sublayers of the $[M_2LiO_6]^{3-}$ layers while (the for delafossites) typical equal–equal transitions AA, BB and CC are achieved by any of the three different $\mathbf{s}_i$ vectors. With respect to the Li and M atoms three-dimensionally ordered polytypes – all having the mentioned $3R$ delafossite type stacking with respect to the O atoms – can be derived by ordered occurrence of the $\mathbf{s}_i$ vectors. The simplest of these polytypes have the symmetries $P3_112/P3_212$ (cyclic sequence of the $\mathbf{s}_i$ vectors; the test structure considered for the TEM data in section), $C2/m$ (occurrence of only one of the three $\mathbf{s}_i$ vectors) and $C2/c$ (alternate occurrence of two out of the three $\mathbf{s}_i$ vectors). These polytypes, however would give rise to superstructure reflections which should be well detectable in the XRPD patterns.

It is interesting to note that stacking of the octahedral layers using $-\mathbf{s}_i$ vectors instead of $+\mathbf{s}_i$ vectors yields, with respect to the O atoms, a cubic close packing ---ABCA---. Upon considering then a honeycomb ordering within these stacked layers, simple stacking variants occur, which can be regarded as analogs (with same space group types) of those just derived for the $3R$ delafossites. Such variants have indeed been reported for compounds like Li_2SnO_3, Li_5ReO_6, V_6C_5 and Pd_6B [22].

5. Conclusions

The real structures of the new quaternary delafossites $Ag(Li_{1/3}Rh_{2/3})O_2$ and $Ag(Li_{1/3}Ir_{2/3})O_2$ have been analyzed, and the diffuse scattering as monitored by X-ray powder and electron diffraction has been qualitatively rationalized by assuming severe disorder in the stacking sequences of the $[M_2LiO_6]^{3-}$ layers (M=Rh, Ir). The presence of an irregular stacking can be regarded as a direct consequence of the route of synthesis applied. During the topochemical transformation of the ordered rock salt variants Li_2MO_3 to the quaternary delafossites $Ag(Li_{1/3}M_{2/3})O_2$ by ion exchange the oxygen atom layer stacking sequence needs to change from ---ABCA--- to ---AABBCCAA---. The respective shortest distance

moves are triply degenerate, and may occur with equal probability, which is resulting in an apparently random stacking sequence as seen with integrating probes.

Appendix A. Supporting information

Supplementary data associated with this article can be found in the online version at doi:10.1016/j.jssc.2011.03.014.

References

[1] A. Pabst, Am. Mineral. 31 (1946) 539–546.
[2] R.D. Shannon, D.B. Rogers, C.T. Prewitt, Inorg. Chem. 10 (1971) 713–719.
[3] B.U. Kohler, M. Jansen, Z. Anorg. Allg. Chem. 543 (1986) 73–80.
[4] E. Wawrzynska, R. Coldea, E.M. Wheeler, T. Soergel, M. Jansen, R.M. Ibberson, P.G. Radaelli, M.M. Koza, Phys. Rev. B 77 (2008) 094439-1-14.
[5] M. Poienar, F. Damay, C. Martin, J. Robert, S. Petit, Phys. Rev. B 81 (2010) 104411-1-8.
[6] A. Maignan, C. Martin, R. Fresard, V. Eyert, E. Guilmeau, S. Hebert, M. Poienar, D. Pelloquin, Solid State Commun. 149 (2009) 962–967.
[7] S. Saadi, A. Bouguelia, A. Derbal, M. Trari, J. Photochem. Photobiol. A-Chem. 187 (2007) 97–104.
[8] Y. Hosogi, H. Kato, A. Kudo, J. Mater. Chem. 18 (2008) 647–653.
[9] V.B. Nalbandyan, Russ. J. Inorg. Chem. 45 (2000) 1652–1658.
[10] H.M. Rietveld, J. Appl. Crystallogr. 2 (1969) 65.
[11] TOPAS, Bruker AXS, Karlsruhe, Germany.
[12] M.M.J. Treacy, J.M. Newsam, M.W. Deem, Proc. R. Soc. London A 433 (1991) 499–520.
[13] A. Avilov, K. Kuligin, S. Nicolopoulos, M. Nickolskiy, K. Boulahya, J. Portillo, G. Lepeshov, B. Sobolev, J.P. Collette, N. Martin, A.C.R. Fischione, P. Fischione, Ultramicroscopy 107 (2007) 431–444.
[14] R. Vincent, P.A. Midgley, Ultramicroscopy 53 (1994) 271–282.
[15] P.A. Stadelmann, Ultramicroscopy 21 (1987) 131–145.
[16] Emap 1.0, AnaliTEX, Stockholm, Sweden, 2002–2007.
[17] P.W. Stephens, J. Appl. Crystallogr. 32 (1999) 281–289.
[18] A. Leinweber, J. Appl. Crystallogr. 39 (2006) 509–518.
[19] B.E. Warren, Phys. Rev. 59 (1941) 693–698.
[20] L. Kienle, M. Schlosser, M.J. Manos, C.D. Malliakas, V. Duppel, C. Reiner, H.J. Deiseroth, M.G. Kanatzidis, K. Kelm, A. Simon, Eur. J. Inorg. Chem. (2010) 367–378.
[21] M. Jansen, R. Hoppe, Z. Anorg. Allg. Chem. 408 (1975) 104–106.
[22] G. Lang, Z. Anorg. Allg. Chem. 348 (1966) 246–252;
J. Hauck, K. Mika, Prog. Solid State Chem. 28 (2000) 1–200;
N.V. Tarakina, T.A. Denisova, L.G. Maksimova, Y.V. Baklanova, A.P. Tyutyunnik, I.F. Berger, V.G. Zubkov, G. van Tendeloo, Z. Kristallogr. Suppl. 30 (2009) 375–380;
A.I. Gusev, A.A. Rempel, J. Phys. C: Solid State Phys. 20 (1987) 5011–5025;
T.G. Berger, A. Leineweber, E.J. Mittemeijer, C. Sarbu, V. Duppel, P. Fischer, Z. Kristallogr. 221 (2007) 450–463.